Temperature dependent and time resolved photoluminescence of $MoTe_2$, MoS_2 and WSe_2

Master thesis in solid state physics at the
University of Zürich

With experimental work carried out at the
University of Amsterdam (UvA)

Author
Kevin Kramer

Supervisor
Prof. Dr. A. Schilling

Local supervisor UvA
Dr. A. Capretti

February – November 2017

Abstract

This master thesis presents measurements and results on three representants of two-dimensional (2D) (i.e. atomically thin in one direction) transition metal dichalcogenides (TMDCs). This family of materials exhibits properties which make them promising candidates for progress in many fields, such as optoelectronics, photodetection, photovoltaics, sensing and to study physical phenomena such as many body interactions [1]. Here, temperature dependent and time resolved photoluminescence (PL, TRPL) studies have been undertaken on monolayer $MoTe_2$, MoS_2 and WSe_2. Among the most important results is the observation of biexcitons in MoS_2 under high excitation power, consistent with a recent report [2], the affirmation of the indirect nature of the bandgap in WSe_2 as well as a deeper understanding of the radiative and non-radiative decay channels for excited electrons in this system.

Contents

1 Introduction

The present thesis concerns itself with investigations on a specific group of materials, the 2D TMDCS. Optical measurements such as linear absorption, PL and TRPL were carried out on three representants of this group over the course of this project. This introductory section attempts to provide a motivation as to why the carried out experiments are of interest. Even though the link between the actual measurements undertaken and technological advancements in the improvement of photovoltaics and solar power generation is of a rather indirect nature, this sustainable method of energy generation is of personal interest to the author and thus we start motivating our work by talking about the limitations of current photovoltaic systems and how 2D TMDCS could help overcome these limitations. This is followed by a short overview on 2D TMDCs in general. Section 2 explains the experiments that were carried out and what methods and hardware was used in the process before section 3 presents the obtained results and complements the presentation with discussion and explanation.

1.1 Solar power generation

The irradiation to current conversion efficiency of present-day commercial Si based solar cells is theoretically limited by Shockley and Queisser's *detailed balance limit* at around 30 % [3]. A big contribution to this strong limitation is due to the fact that only incoming photons whose energy $h\nu$ equals the bandgap of Si $E_g = 1.12\,\mathrm{eV}$ can be converted efficiently. If the photon energy is greater than E_g, the excess energy is converted to heat through fast thermalization of the excited electron. If $h\nu < E_g$, however, no electron can be lifted above the bandgap and the photon energy cannot be used at all. A visual representation of how much of the solar spectrum could be used by an ideal Si solar cell is given in figure 1.

It should be mentioned that even with the relatively low efficiencies of modern commercial photovoltaic systems, the economically relevant measure of cost per kW h for solar energy has been going down and has begun to be competitive with the costs for non renewable technologies [4–6]. Nevertheless, overcoming the Shockley-Queisser limit and increasing the efficiency of solar cells is a goal which would greatly help to reduce the cost of solar energy further and to make this renewable technology a dominant figure in the energy generation landscape.

One approach to this end is the combination of different materials with complementary spectral efficiency profiles in a single cell. Four-junction devices have reached a record efficiency of 46 % in solar concentrator conditions [7]. These tandem systems, however, are much more complex to assemble and thus have a much higher cost of fabrication. While not directly aiming at overcoming the Shockley-Queisser limit, perovskite based solar cells [8] are much cheaper to produce than conventional semiconductor based

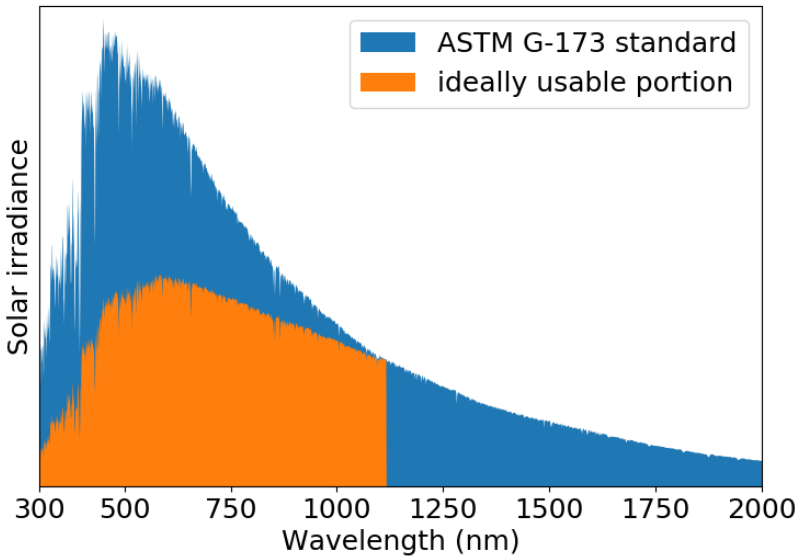

Figure 1: Solar spectrum according to the international standard ASTM G-173 (AM1.5G) and the portion of it which could be used by an idealized solar cell with $E_g = 1.12\,\mathrm{eV}$. Below the Si bandgap at 1100 nm a decreasingly small fraction of the spectrum can be used, while the whole tail above it remains completely unused.

systems making them an attractive competitor.

A more direct approach at accessing the inefficiently converted parts of the spectrum (cf. figure 1) is by making use of up- and downconversion mechanisms. Upconversion labels a process by which two lower energy photons are absorbed and one of higher energy is emitted. The opposite process where one high energy photon is used to generate several lower energy photons is called downconversion. In this way, infrared (IR) photons which pass through a conventional solar cell could be combined to photons above the bandgap energy and thus be absorbed. Likewise, high energy photons could be "cut" to multiple photons closer to E_g such that their energy is converted more efficiently and heat losses are minimized. Promising candidate materials in which these processes could occur include nanocrystals or two-dimensional materials [9]. Particulary, the 2D TMDCs with their tunable bandgaps and the possibility to produce atomically thin layers have been repeatedly proposed to this end.

1.2 Two-dimensional transition metal dichalcogenides

TMDCs are a class of materials with the formula MX_2 where M is a transition metal from groups IV, V or VI and X is a chalcogen (S, Se or Te). The

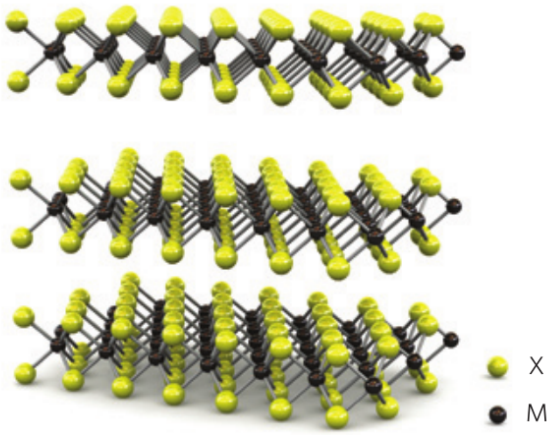

Figure 2: Structure of a TMDC. The chemically bonded X–M–X layers are held together by van der Waals forces in bulk. Figure from [1].

materials form stacked layers of the form X–M–X (cf. figure 2) which are held together by van der Waals forces to form the bulk crystal.

Stacked materials like this can be exfoliated down to single layers [10]. In this way it is possible to create a 2D version of a layered material which often exhibits different properties from its bulk form. This is also the case for the 2D TMDCs. They have been extensively reviewed by [1] and [11] so we will only give a short overview on this family of materials, focusing on the aspects relevant to work presented here.

As just mentioned, 2D TMDCs are particularly interesting because they exhibit a range of properties that can differ significantly from their bulk forms. The most notable here is that semiconducting TMDCs (MoX_2 and WX_2) have an indirect bandgap in bulk which gradually shifts towards a direct bandgap in the monolayer limit [12]. This is shown in figure 3 for the example of MoS_2 where we see density functional theory calculations of the band structures at different thicknesses. In the case of MoS_2 the transition is explained through the nature of the different orbitals that contain electronic states involved in the direct and indirect gap transitions. The states at the direct gap primarily live in strongly localized d orbitals at the Mo sites. As the Mo atoms are located in the middle of the S–Mo–S unit cell, these orbitals exhbit little interlayer coupling. States at the indirect gap, however, come from hybridized S p_z and Mo d orbitals which have strong interlayer coupling and therefore their energies depend strongly on the number of layers [13, 14].

This transition happens for all semiconducting TMDCs, which have bandgaps in the range of 1.1 eV to 2.1 eV as monolayers. An important consequence of the change to a direct band gap is the emergence of strong photoluminescence (PL) in these materials. MoS_2, for example, shows an increase in PL quantum yield by a factor of 10^4 between single layer and bulk [13]. The availability of a range of bandgaps and the possibility to tune these gaps by layer thickness and through intercalation, thus changing the interlayer distance [15], make these materials good candidates for

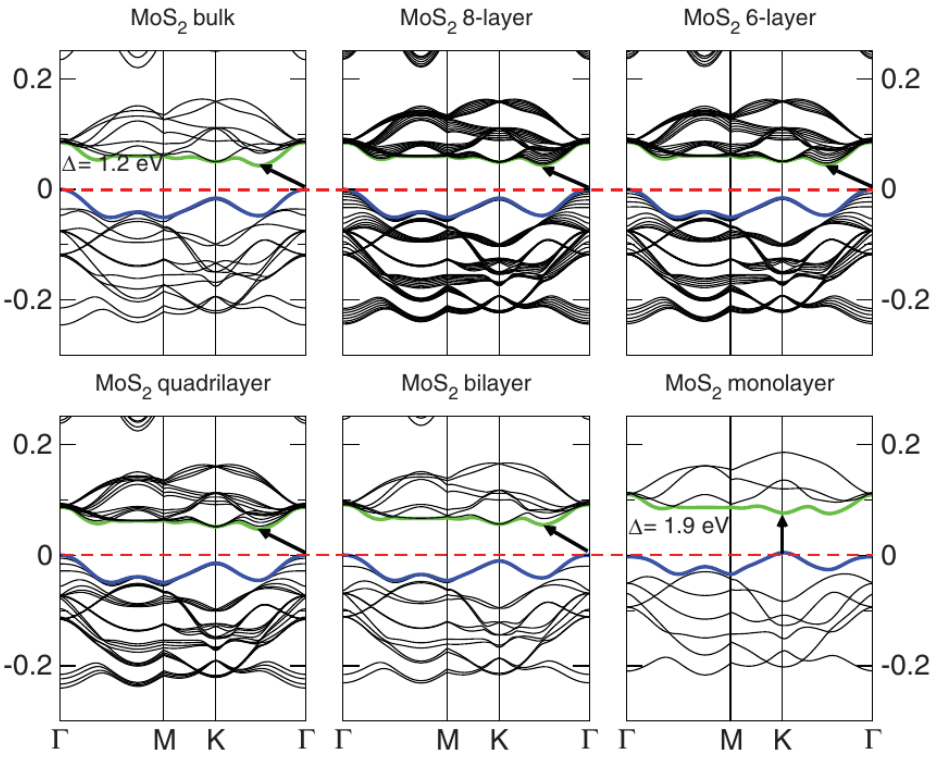

Figure 3: DFT band structures of MoS_2 in bulk and few-layer forms. The ratio of energies at the Γ point with respect to the K point gradually decreases until the initially indirect bandgap of 1.2 eV shifts to a direct gap of 1.9 eV. Figure from [12].

photovoltaic, optoelectronic and photodetection applications.

Furthermore, the exciton binding energy in these materials is typically quite large with values in the range 200 meV to 800 meV. In this way, they provide a platform for the study of many-body interactions, i.e. the formation of bound states of electrons and holes with more than two participants like trions (two electrons and a hole or two holes and an electron) and biexcitons (two electron–hole pairs) [2, 16–20].

2 Experimentals

2.1 Used components

Different combinations of excitation sources, detectors and other components were used in order to measure different optical properties of the investigated materials. This section gives an explanation over some of the more important parts of the used setups.

2.1.1 Optical parametric oscillator

An optical parametric oscillator (OPO) generates coherent light pulses of variable wavelength. The used system is driven by a Nd:YAG laser which creates nanosecond pulses at the fundamental lasing wavelength of 1064 nm. By means of nonlinear processes the third harmonic of this wavelength is generated and fed into a beta-barium-borate crystal where a second-order nonlinear effect takes place, splitting the pump photon into two lower energy photons, historically called the 'signal' and the 'idler' waves. The ratio between signal and idler wavelengths in this process is dependent on the angle between incident light and crystal orientation, thus rotating the crystal allows for the creation of pulsed light in the range of 210 nm to 2480 nm. Signal or idler can then be used as the excitation source for an experiment.

2.1.2 Cryostats

Two types of cryostats have been used in this thesis: a continuous flow cryostat (CFC) and a closed cycle cryostat (CCC). In both systems the sample is in thermal contact with a cold finger which is being cooled by a steady flow of liquid helium at 4.2 K. In the CFC the helium is supplied from a storage dewar and the used, evaporated helium is transferred out of the system. The flow of the helium can be adjusted through needle valves on the supply side or at the suction pump end. In this particular setup, the thermal contact between sample and cold finger is realized by using dry helium as an exchange gas. The CCC, on the other hand, recycles the evaporated gas and cools it back down in an external refrigerator. Here, there is no control over the gas flow but in both setups temperature can be controlled by a simple electric heater which is regulated by an Edinburgh Instruments ITC503 temperature controller.

2.1.3 Detection systems

Various detection systems are used depending on the type of experiment and the spectral range of the emission. In most cases, a diffraction grating is necessary to select a portion of the spectrum. These gratings, each with their own optimized wavelength, are integrated in commercial spectrometers (Solar M266, Horiba Jobin Yvon SPEX1000M). CCD cameras and a

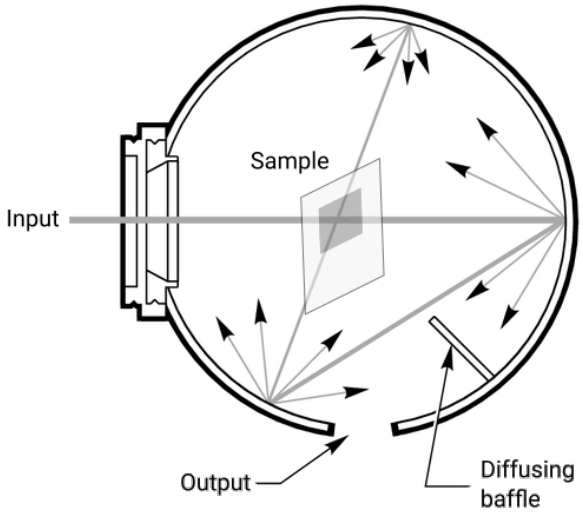

Figure 4: Schematic representation of an integrating sphere. The inside is coated with a diffusively reflective surface, principally ensuring that all incoming light gets reflected repeatedly off the sphere wall until it eventually reaches the detector (*Output*).

liquid nitrogen cooled Edinburgh Instruments Germanium detector coupled to a lock-in amplifier (Signal Recovery SR7265) allow measuring the time-integrated PL spectra for visible or near-IR (NIR) emission respectively. A photomultiplier tube (PMT) is used in the TRPL experiments.

2.2 Linear absorption

In order to measure the linear absorption of the investigated materials an integrated system (Perkin Elmer Lambda 950 spectrometer) was used. It is equipped with a tungsten-halogen and a deuterium lamp and a PMT detector for the visible range and a PbS detector for the NIR. An integrating sphere is used in this setup to account for scattering effects. The samples are mounted in the center of the integrating sphere in such a way that they are hit by the incoming probe beam through the sphere's entrance opening without directly reflecting light back out of the sphere. The amount of scattered light that is lost through the entrance opening can be estimated by performing a scan of an empty sphere, with no sample in place. The white coating of the sphere's inside ideally reflects all scattered and reflected light from the sample repeatedly until it eventually reaches the exit to the detector. This means, however, that multiple pass absorption may occur, thus the absorption measured in this setup is generally slightly overestimated.

2.3 Temperature dependent photoluminescence

Electrons in a typical semiconductor can reach an energy state in the conduction band (and leaving a hole in the valence band) by absorbing a photon with photon energy $h\nu$ greater or equal to the band gap energy E_g. Once in this excited state, in which the the electron energy is typically higher than

the band edge, it may lose its excess energy by interacting with the crystal lattice, i.e. through thermalization. This process happens on the timescale of picoseconds or faster. Once the charge carriers have relaxed to the edge of the conduction band (or valence band for holes), they can cross the band gap and return to their ground state by emitting a photon (radiative recombination, timescale of micro– or nanoseconds) [21]. The emitted light (PL) can be detected with the setup described in this section and the timescales involved can be measured with TRPL, cf. next section.

A schematic representation of the setup to measure the temperature dependent PL is shown in figure 5. An OPO, a continuous wave laser or a Xenon lamp are used as excitation source. The excitation beam is guided via silver coated optical mirrors onto the sample, which is located in the sample chamber of the cryostat. The sample is aligned at such an angle to ensure that the excitation beam is not directly reflected towards the light collection on the emission side. A pair of lenses is used to focus the emitted light through the monochromator onto the detector's active area. Suitable filters are incorporated in the setup in order to get rid of remnants of the excitation which include the set excitation wavelength itself, the OPO's idler wavelength and the unwanted transitions coming from the driving Nd:YAG laser (or others depending on the used source).

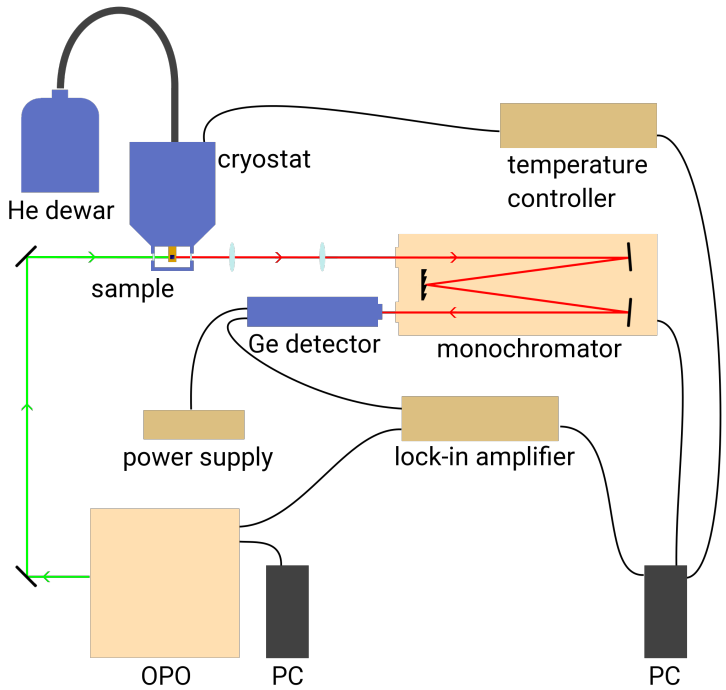

Figure 5: Scheme of the T-dependent PL setup for the example of infrared emission. For visible emission a CCD or a PMT sensitive to visible light are used instead of the Ge detector–lock-in combination.

2.4 Time resolved photoluminescence

In order to measure the recombination lifetimes of excited states, a pulsed source has to be used. The pulse repetition rate is such that the PL signal decays long before the next pulse hits the sample material. After the pulse has excited the sample, the system is left to relax back to its equilibrium state and the photons emitted during this period are recorded with their arrival times. For very fast decays with time constants below a few nanoseconds it is hard or even impossible for the readout electronics to keep up with the incoming data. However, it is still possible to acquire decay times in the order of picoseconds or lower (limited by the excitation pulse length) by employing time correlated single photon counting (TCSPC). In this mode, one attenuates the intensity of the signal so much, that the probability of detecting two or more photons per pulse is negligibly low. This means that in most pulses one will not detect any photons at all but there will be some cycles with a single photon present. The histogram of the arrival times of the so detected photons is ideally identical to the histogram one would have gotten in a 'single shot' measurement.

Though the system used in this thesis is equipped with TCSPC mode, it could not be used as the driving fast pulsed laser emits at 355 nm which excites the quartz substrate. Because of this, TRPL measurements were only done in the regime where the electronics can capture the full decay immediately, using an OPO at 10 Hz repetition rate and leading to a time resolution of 20 ns.

3 Results

This thesis concerns itself with three samples which were all supplied by a collaborating group [22]. One sample consists of circa twenty layers of $MoTe_2$ on an Si substrate and will be referred to as *the $MoTe_2$ sample*. The other samples have a thickness of one to two layers and were grown on an α-quartz substrate. The respective materials are WSe_2 and MoS_2. All samples were grown using a vapor phase reaction method [2]. The samples were stored in vacuum whenever no experiments were performed on them to prevent degradation.

In the following we give an overview of the measurements undertaken for each sample and present the acquired data and results. All experimental and analytical results of this section, if not referenced or explicitly stated otherwise, were acquired by the author.

3.1 $MoTe_2$

The $MoTe_2$ sample did not show any PL at room temperature (RT). When going to low temperatures (LT) the PL starts to slowly set in, increasing steadily until it reaches its highest intensity at circa 50 K after which it decreases again. Though this behaviour appears to be quite interesting and would warrant further investigation, a subsequent experiment clearly showed that the observed PL signal does not stem from the $MoTe_2$: An empty substrate, identical to the one the $MoTe_2$ is grown on, has been put in the exact identical setup and measured under identical conditions. The result was that the exact same spectra with the same temperature dependence were observed as can be seen in figure 6. A bare piece of polished Si was measured in the same way and led to the same results yet again, indicating that the observed spectra indeed stem from Si and are not intrinsic to our substrate.

After reaching the conclusion that we are unable to detect any PL from this sample, no further investigations were undertaken.

3.2 MoS_2

3.2.1 Absorption

The recorded absorption spectrum of the MoS_2 sample is given in figure 7. The observed features can be clearly identified with the help of band structure calculations [16], figure 8. The spin-orbit coupling induced splitting of the valence band [23] leads to there being two direct bandgap transitions A' and B'. Similarly, there are also two excitonic transitions A and B. The difference between the A and A' as well as between the B and B' preaks is the exciton binding energy, typically so large in 2D TMDCs [20]. Calculated

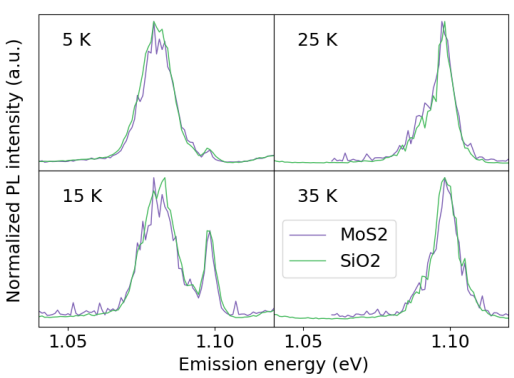

Figure 6: Recorded spectra of the $MoTe_2$ sample and the bare Si substrate at low temperatures. The spectra are almost identical in shape indicating that the whole signal stems from the substrate itself and there is no appreciatable PL from the $MoTe_2$.

and measured values for these transitions along with the result one gets from the here measured absorption spectrum are summarised in table 1.

Our values for the A and B transitions perfectly match previous experimental results [13] and are in good agreement with the calculations. There is, however, a small discrepancy between the calculations and the observed values for the A' and B' transitions and consequently for E_{exc}. We assume that the calculations overestimate E_{exc} as the used approximation is on the border of its applicability, as is stated by the authors[16].

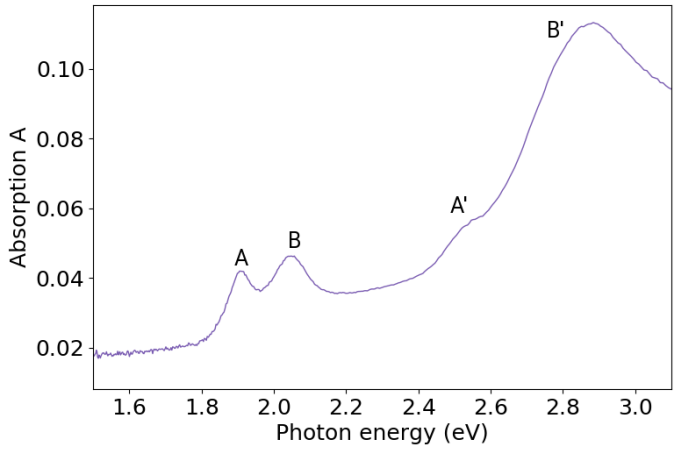

Figure 7: Absorption of the monolayer MoS_2 sample. Features are labeled following the nomenclature of Wilson and Yoffe [24]. The absorption is given in absolute units, i.e. 1 corresponds to 100 % absorption.

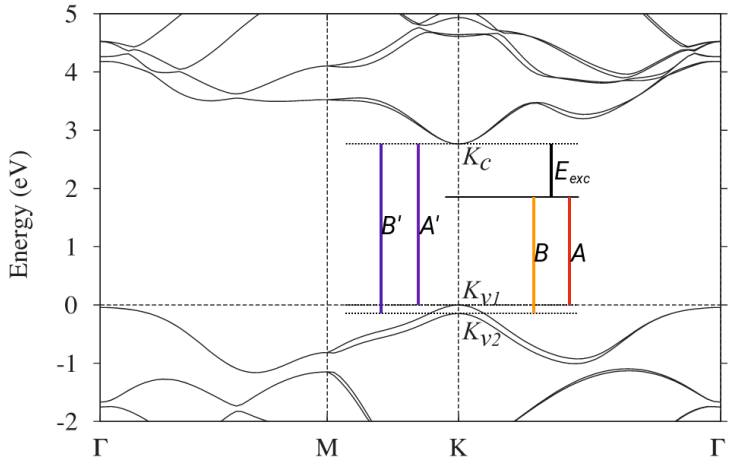

Figure 8: Calculated band structure of monolayer MoS_2. The exciton binding energy E_{exc} as well as the excitonic and direct transitions are labeled. Figure adapted from [16].

(eV)	A	B	A'	B'	E_{exc}
Theory [16]	1.86	2.01	2.76	2.91	0.897
Measured [13]	1.9	2.05			
Measured here	1.9	2.05	2.56	2.88	0.75

Table 1: Calculated (*Theory*) and by means of absorbance measurements deduced values for different transitions in MoS_2.

3.2.2 Temperature dependent photoluminescence

The obtained data from PL measurements on MoS_2 at RT and below is visualized in figure 9. The used excitation source was an OPO at 450 nm, at a pulse frequency of 100 Hz and the laser power was measured to be 70 mW. The beam spot was not completely focused on the sample, however, and thus the estimated deposited power density was $(2 \pm 1)\mathrm{mW\,mm^{-2}}$.

One can see that the PL intensity increases steadily with decreasing temperature and the peak position remains at 1.84 eV for all measured temperatures. A broad feature with center around 2.2 eV appears below 200 K and grows at a comparable rate as the main PL peak. To gain a better understanding of this behaviour, the ratio between the PL intensity of this broad feature and the main peak is plotted in figure 10. One can see that the feature becomes more prominent from below 250 K until it is fully developed with respect to the overall PL intensity at 175 K. Towards the lower energy side of the main peak another broad feature is visible. It also grows faster than the main peak but at roughly the same pace over the full temperature range.

Discussion. MoS_2 PL has been measured many times before. A collec-

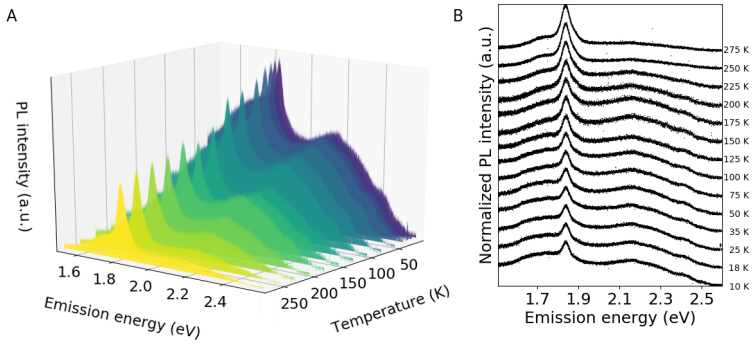

Figure 9: Results of PL measurements on MoS_2 at different temperatures. The two plots show the same data but the spectra in **B** have been normalized and vertically offset. One can see from the unnormalized data in **A** that the PL intensity increases steadily with decreasing T while we can see in **B** that the main peak does not move with T and the shape of the spectra is very similar for all temperatures.

tion of results from various references can be found in figure 11. The values range from 1.85 eV to 1.9 eV and the mean value for the excitonic peak from this data lies at around 1.89 eV, 40 meV above our result of 1.84 eV. Our result also lies 60 meV below the measured absorption peak for the excitonic transition. A possible explanation for this discrepancy could be linked to the recently observed tri– and biexciton generation in MoS_2 [2]: Lee and coworkers measure MoS_2 PL spectra at different gating voltages and excitation powers (the sample used by Lee is put on a SiO_2/Si substrate, however, so one has to keep in mind that there is a slim possibility of the substrate influencing the behaviour thus making the following findings not applicable to our case). They observe a broadening of the peak towards lower energies with increasing power as well as with increasing gate voltage (figure 12) and explain this by increased (negative) trion and biexciton formation due to the higher availability of free carriers and thus higher probabilities of forming multiexcitonic states. In other words, the peak is not just getting broader, but rather does it consist of three separate peaks: the excitonic at $P_0 = 1.90\,\text{eV}$, the trionic at $P_1 = 1.87\,\text{eV}$ and the biexcitonic at $P_2 = 1.84\,\text{eV}$. One can see that at the highest probed power of 500 µW the contribution of multiexcitons to the total PL is greater than that of the single exciton and the peak appears to have shifted to lower energies. In our experiment, the laser power was an order of magnitude higher than the reported situation, leading to the interpretation that we are in a situation where the PL emission is dominated by biexcitonic transitions. This would be consisted with the reported value for the biexciton peak of $P_2 = 1.84\,\text{eV}$.

We assign the broad feature around 2.2 eV with the excitonic B transition as it matches its energy quite well and there have been reports of the B peak being significantly less intense than the A peak [2, 25]. The lower energy feature has also been observed before [25]. Its origin remains unclear at this

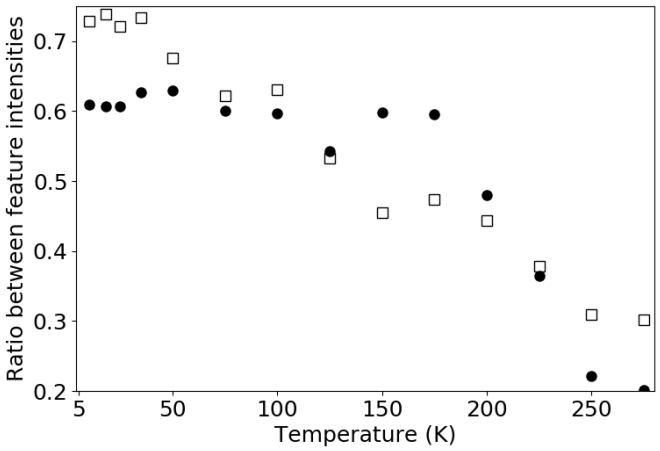

Figure 10: Ratio between the intensities of the broad feature (F) around 2.2 eV (black circles) or the presumed B peak around 1.7 eV (white squares) and the main peak (A) at 1.84 eV respectively. F grows with respect to the peak from 250 K to 150 K and stabilizes there while the B peak continually grows faster than the main peak.

point.

3.2.3 Time resolved photluminescence

Attempts at measuring TRPL of the MoS_2 sample only resulted in the observation of a decay below the limit of the available systems of a 20 ns. We can thus only provide this number as an upper bound for the decay time, which at least is consistent with expected and reported decay times in the order of picoseconds or below [25, 26].

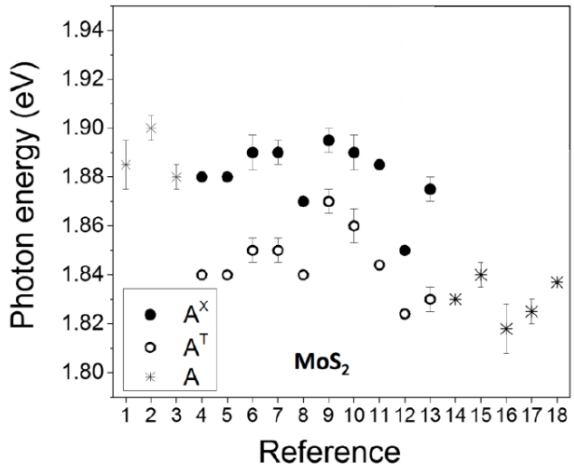

Figure 11: Peak positions for the excitonic (A^X, solid circles), trionic (A^T, open circles) and unassigned (A, stars) PL peaks as reported by different references. Figure adapted from [2].

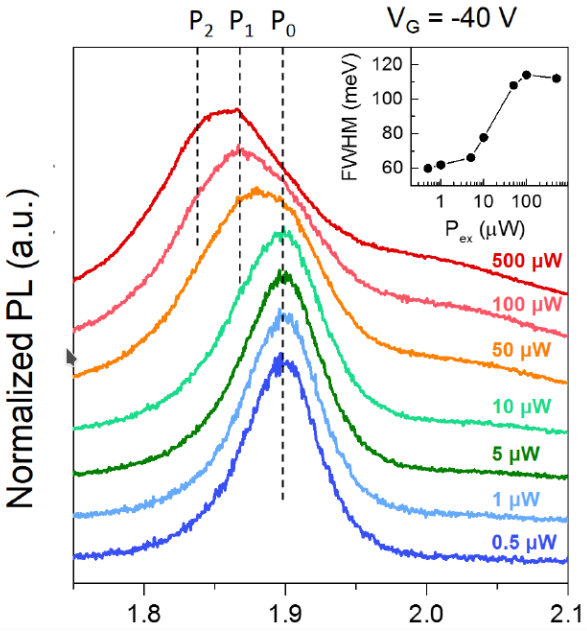

Figure 12: Room temperature PL spectra for MoS_2 at constant gate voltage and varying excitation powers. The peak broadens with higher powers i.e. higher availability of free carriers. This is explained by an increasing amount of tri– and even biexcitons forming, which have a higher binding energy and thus lead to lower energy PL emission. Figure from [2].

3.3 WSe_2

3.3.1 Absorption

Figure 13 shows the absorption spectrum obtained from the WSe_2 sample and figure 14 shows the result of an LDA calculation for the bandstructure of single layer WSe_2 [27]. As reported in other places [28, 29], single layer WSe_2 has an indirect gap, as opposed to most other 2D TMCS. Some values for the energy differences between labeled points in the shown band structure are collected in table 2.

The value from the valence band splitting ($K_{V,A} \rightarrow K_{V,B}$) matches the difference between the first two peaks and the last two respectively, indicating that we are presented with the same A, B, A', B' situation as was the case for MoS_2 (section 3.2.1). One has a hard time, however, fitting the other LDA values into the picture. We assume that the LDA calculation significantly underestimates the bandgap and tentatively assign peaks in the absorption spectrum as follows: Direct excitonic A peak: 1.68 eV, direct excitonic B peak: 2.10 eV, direct gap A' ($K_{V,A} \rightarrow K_C$): 2.50 eV and the direct gap B' transition ($K_{V,B} \rightarrow K_C$): 2.92 eV. This assignment is consistent with values found in [26].

We note that these peaks stem from the direct gap transitions. Their absorption is weaker than it was the case for the MoS_2 sample, owing to the indirect nature of the material. It is clear from the absorption spectrum and the band structure calculations, however, that the energy difference between the direct and indirect gaps is very small and thus that both play a role in the physics of WSe_2.

(eV)	$K_{V,A} \rightarrow K_{V,B}$	$K_{V,A} \rightarrow K_C$	$K_{V,A} \rightarrow C_{min}$
LDA	0.454	1.47	1.35
ARPES	0.513		

Table 2: Calculated and by means of APRES obtained values for some transitions in monolayer WSe_2. Values taken from [27].

3.3.2 Temperature dependent photoluminescence

The PL of the monolayer WSe_2 sample has been measured under similar conditions as for MoS_2 (section 3.2.2), though the used excitation source was a 532 nm continuous wave laser. The results can be found in figure 15. Measurements with the same OPO as for MoS_2 have also been undertaken to ensure that the PL is unaffected by the choice of excitation source. The RT peak at 1.68 eV continually blueshifts with decreasing temperature while also growing in intensity. From 200 K and below the intensity of this RT peak starts to decrease and a new peak (low temperature (LT) peak) appears at lower energy, below 1.6 eV, which quickly grows in intensity to a factor of 10 from the maximum of the higher energy RT peak, completely dominating

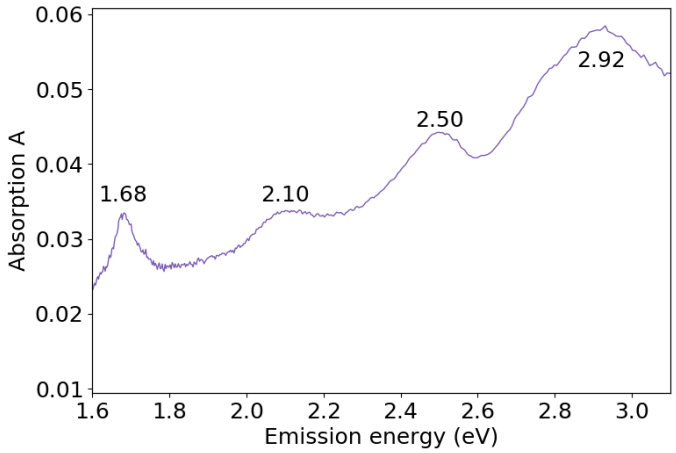

Figure 13: Absorption spectrum for the WSe_2 sample. Absorption is given in absolute values, i.e. 1 corresponds to 100 %. Peaks have been annotated with their respective energy in eV.

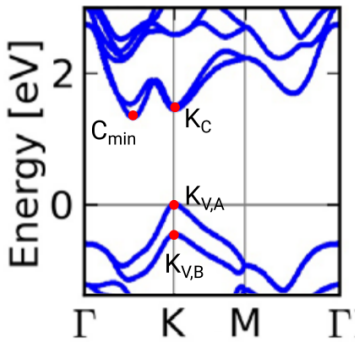

Figure 14: LDA band structure of monolayer WSe_2. The results indicate an indirect gap semiconductor. The conduction band minimum (C_{min}), the local minimum at the K point (K_C) as well es the split valence band maxima ($K_{V,A}$, $K_{V,B}$) have been labeled. Figure adapted from [27].

the spectrum below 100 K and 'swallowing' the RT peak. This behaviour is visualized more clearly in figure 16.

We note that the RT PL spectrum looks very different from what can be found in literature [18, 30] where we can see four distinct, sharp peaks in the energy range 1.65 eV to 1.75 eV. Another reference [31], on the other hand, is in agreement with the spectra presented here. The difference must be related to the different sample preparation methods that were employed: the spectra with the four sharp peaks stem from samples which were mechanically exfoliated [10] while chemically grown samples seem to lead to a single peak spectrum. Clearly, the preparation methods result in different crystal lattice phases [32, 33] which exhibit different PL.

Discussion. A tentative explanation for the observed behaviour of the T-dependent PL is as follows: we assume that there are three possible relax-

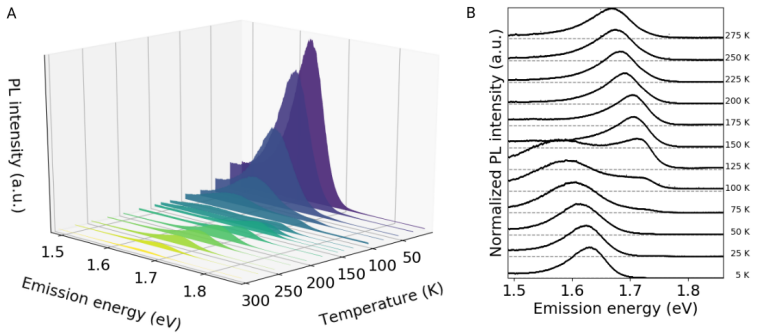

Figure 15: Results of PL measurements on WSe_2 at different temperatures. The two plots show the same data but the spectra in **B** have been normalized and vertically offset. A new peak starts appearing below 150 K and dominates the low temperature PL.

ation pathways for a photoexcited electron in the conduction band. First, the non-radiative pathway (NR) whereby the electron transfers its energy to lattice vibrations and/or defects and relaxes without emitting a photon. We assume that the probability for NR is a function of the temperature. Second, the indirect pathway (IN) where an electron from the bottom of the conduction band (C_{min}) exchanges momentum with a phonon allowing it to move to the top of the valence band at K, thereby emitting a photon at the energy of the indirect gap (minus the exciton binding energy E_{exc}). Finally, the direct pathway (D) in which an electron at K_C transitions over the direct bandgap to the valence band maximum, emitting a photon at the bandgap energy (minus E_{exc}). The emission from IN is at slightly lower energy than the one of D, as we are in an indirect semiconductor. At RT, most electrons decay via NR and only a small portion is able to emit light via D, owing to the relatively weak RT peak. The LT peak sets in as the rate for an electron to decay via IN becomes comparable to NR and electrons start to emit at slightly lower energies via this indirect pathway. At decreasing T, the probability for NR decreases further until the spectrum is dominated by IN. In order to concretize and validate this model we require the results from TRPL measurements in the following section.

3.3.3 Time resolved photoluminescence

The observed dynamics of the PL at low temperatures typically show a very fast decay which is below the resolution of the used system (20 ns) followed by a slow tail with a decay constant in the order of µs. Above 20 K one can see that the slow component starts to get weaker until it does not contribute anything to the PL anymore at 108 K and above (figure 17). Furthermore, the dynamics at a specific temperature were compared for different emission energies: one which corresponds to the RT peak and the

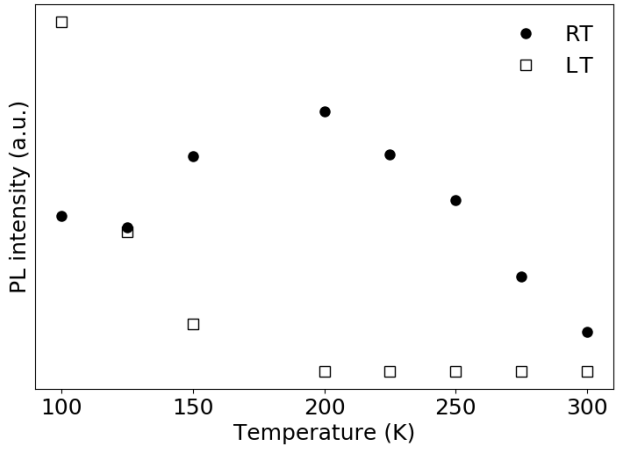

Figure 16: Intensities of the RT and the LT peaks. One can see how the RT peak grows from 300 K to 200 K before it decreases in favour of LT peak, which quickly starts dominating the spectrum. The RT point at 100 K shows how the RT peak is being 'swallowed' by the LT peak.

other which corresponds to the LT peak (figure 18). One can see that the RT PL does at most contain 10 % as much signal from the slow component compared to the LT peak. Figure 19 illustrates how the slowly decaying component, when it is present, contributes a large fraction to the total PL at a given emission wavelength.

These findings allow us to complete the picture which we started to explain in the previous section. We assign the fast component τ_D to the direct bandgap transition D and the slow component τ_{IN} to the indirect gap transition IN, which is also in accordance with what one would generally expect for decay times of direct versus indirect transitions. As mentioned before, the decay time constant τ_{NR} of the non radiative pathway NR is assumed to be temperature dependent with a trend to increase (i.e. the transition becomes slower) with decreasing T. This assumption is also in accordance with a theoretical model for non-radiative recombination lifetimes in indirect semiconductors, which predicts a $T^{-3/2}$ dependence [34]. Due to this T dependence there is a critical temperature T_C at which $\tau_{NR}(T_C) = \tau_{IN}$. Above T_C the indirect radiative pathway cannot compete with NR and hardly any PL is observed. At and below T_C more and more electrons follow IN and the PL grows accordingly. The situation is illustrated in figure 20.

We note that analyzing the presented data by fitting second order exponentials, as our model would suggest, did not yield satisfactory results and it appears as if a third order exponential is necessary to properly describe the data. Of course, adding more degrees of freedom will generally improve the obtained fit, but figure 21 shows how the improvement when going from

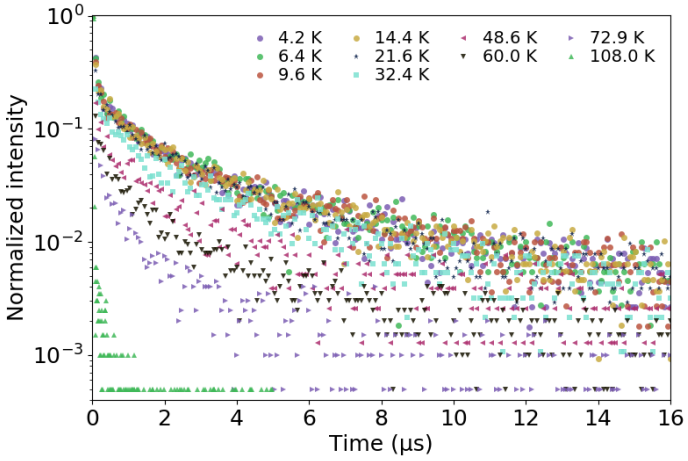

Figure 17: PL decays for the WSe_2 sample measured at the PL peak energy for each temperature. At low temperatures up to 20 K the decays are identical and show a fast, unresolved component followed by a slower compnent with a decay time constant in the order of µs. With increasing temperature the slow component starts to disappear.

second to third order is quite significant, halving the value of χ^2.[1] On the other hand, when going from third to fourth order one only gains a below 1 % improvement in the fit. A stretched exponential,

$$f(t) = A \cdot \exp\left(-\left(\frac{t}{\tau}\right)^{1/h}\right) \quad ,$$

has also been tried to fit the data and it led to an improvement of χ^2 by 10 %. We reverted to the multiple exponential, however, as there is no distinction between 'fast' and 'slow' components in the stretched exponential and it is hard to assign physical meaning to its parameters. We therefore assume that the slow decay τ_{IN} is further composed of two pathways. Possibly these have to do with a splitting of bands near the band edges, as is already the case for the valence band maximum at K or different excitonic states. The splitting of the valence band into A and B, however, is unlikely to be at the origin of this as these states differ too much in energy (section 3.3.1).

[1] $\chi^2 = \sum_i \left(\frac{y_i - f_i}{\sigma_i}\right)^2$, where y_i are the data values, σ_i their uncertainties (in this case the relation for histograms is used that the uncertainty for a bin with N entries is $\sqrt{N}$) and f_i the fit values.

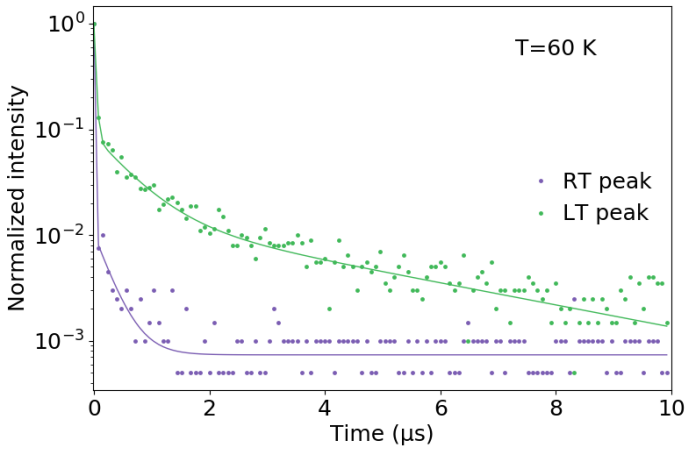

Figure 18: WSe_2 PL decays at $T = 60\,\mathrm{K}$ for the different peaks RT (measured at 1.70 eV) and LT (1.63 eV) which are both visible and distinguishable in the emission spectrum at this temperature. LT clearly contains a slow component while LT does not.

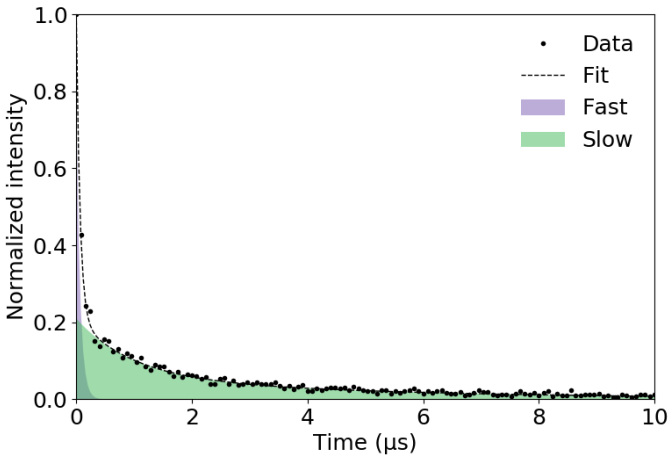

Figure 19: Illustration of the relative contributions of the fast and slow components respectively to the total PL signal. The presented data was acquired at $T = 4.2\,\mathrm{K}$. In this case, the slow component contributes more than 70 %.

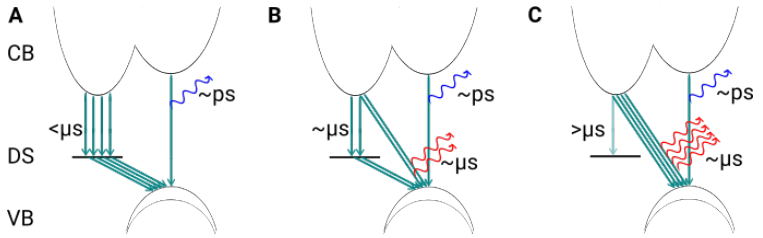

Figure 20: Schematic of decay channels at temperatures above (**A**), near (**B**) and below (**C**) the critical temperature T_C. CB: conduction band, VB: valence band, DS: deep state/ defect state. At high temperatures (**A**) the decay time constant of NR is small and most electrons follow this decay route while a small number very quickly decays via D. The contribution of D is small even though its decay time is very short because thermalisation to the CB minimum is even faster. In **B** the temperature has decreased to a point at which the decay times of NR and IN are comparable and PL emission from NR sets in. Finally, at low temperatures, as depicted in **C**, the NR decay is much slower than IN and most electrons can emit at the LT energy.

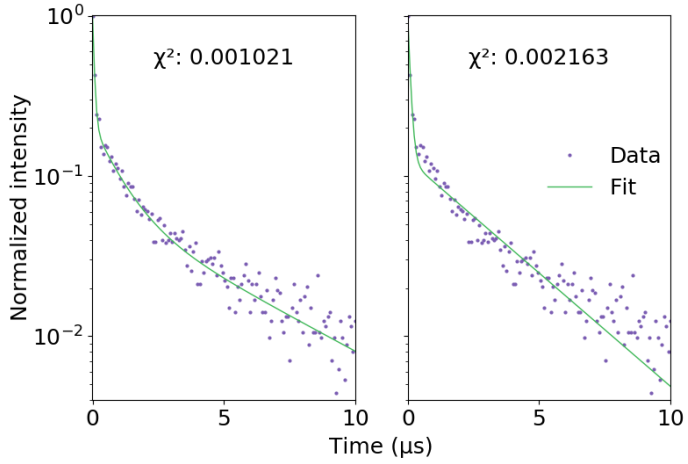

Figure 21: Comparison between a triple and a double exponential fit to the TRPL data at $T = 4.2\,\mathrm{K}$. The triple exponential fits the data significantly better: visually by not exhibiting a 'kink' at below 1 µs and better match of the slope of the slow component and numerically by a halved value for χ^2.

3.4 Summary and outlook

$MoTe_2$. No PL could be detected for the $MoTe_2$ on SiO_2 sample. The expected PL emission for $MoTe_2$ lies just where emission from the substrate occurs, indicating that it may have been overshone by the substrate's emission. We suggest the fabrication of the sample on a non-emitting substrate and the repetition of the experiments in order to get a conclusive result.
MoS_2. The measured PL peak appeared at lower energy than is commonly reported in literature. This might be due to the high excitation power used, which promotes the formation of biexcitons over simple excitons, affirming recent work[2]. The main PL peak hardly shifts with T, as opposed to what is observed in other reports [25]. This may be explained by the biexciton with its higher binding energy being more stable with regard to energy loss to phonons than the exciton. This way the blueshift one usually observes for excitonic transitions at lower temperatures would be suppressed. The PL of the sample could be measured at different excitation powers in order to test this biexciton explanation.
WSe_2. The PL of the monolayer WSe_2 sample shows the typical excitonic blueshift of the RT peak until at a critical temperature $T_C \approx 100\,\mathrm{K}$ a new peak builds up which dominates the spectrum at low temperatures, growing an order of magnitude in intensity compared to the RT peak. To our knowledge, this behaviour has not been reported before. We assign the RT PL to emission from the direct gap transition D while the emerging LT PL is due to the indirect gap pathway winning the competition against the increasingly slower non radiative decay channels. This assignment is backed by TRPL measurements. We thus provide an improvement in understanding of the physics of single layer WSe_2. With further measurements one could now pinpoint the exact value of T_C and the corresponding decay time constant of the slow component which at this point should equal the decay time of NR. By employing a model for the NR decay time temperature dependence ([34]) one could extrapolate the NR decay time constant at RT.

References

[1] Qing Hua Wang et al. "Electronics and Optoelectronics of Two-Dimensional Transition Metal Dichalcogenides." In: *Nature nanotechnology* 7.11 (Nov. 2012), pp. 699–712. DOI: 10.1038/nnano.2012.193. pmid: 23132225.

[2] Hyun Seok Lee et al. "Identifying Multiexcitons in MoS_2 Monolayers at Room Temperature". In: *Physical Review B* 93.14 (Apr. 19, 2016), p. 140409. DOI: 10.1103/PhysRevB.93.140409. URL: https://link.aps.org/doi/10.1103/PhysRevB.93.140409 (visited on 10/16/2017).

[3] William Shockley and Hans J Queisser. "Detailed Balance Limit of Efficiency of P-n Junction Solar Cells". In: *Journal of applied physics* 32.3 (1961), pp. 510–519.

[4] US EIA. "Annual Energy Outlook 2017". In: *US Energy Information Administration, Washington, DC* (2017).

[5] Ivin Rhyne. *Estimated Cost of New Renewable and Fossil Generation in California*. California Energy Commission, 2015.

[6] Christoph Kost et al. "Levelized Cost of Electricity Renewable Energy Technologies". In: *Fraunhofer Institute for Solar Energy Systems ISE* (2013).

[7] F. Dimroth et al. "Four-Junction Wafer-Bonded Concentrator Solar Cells". In: *IEEE Journal of Photovoltaics* 6.1 (Jan. 2016), pp. 343–349. ISSN: 2156-3381. DOI: 10.1109/JPHOTOV.2015.2501729.

[8] Joseph S. Manser, Jeffrey A. Christians, and Prashant V. Kamat. "Intriguing Optoelectronic Properties of Metal Halide Perovskites". In: *Chemical Reviews* 116.21 (2016), pp. 12956–13008. DOI: 10.1021/acs.chemrev.6b00136. pmid: 27327168. URL: http://dx.doi.org/10.1021/acs.chemrev.6b00136.

[9] M.C. Beard and R.J. Ellingson. "Multiple Exciton Generation in Semiconductor Nanocrystals: Toward Efficient Solar Energy Conversion". In: *Laser & Photonics Reviews* 2.5 (Oct. 2008), pp. 377–399. ISSN: 1863-8899. DOI: 10.1002/lpor.200810013. URL: http:https://dx.doi.org/10.1002/lpor.200810013.

[10] KS Novoselov et al. "Two-Dimensional Atomic Crystals". In: *Proceedings of the National Academy of Sciences of the United States of America* 102.30 (2005), pp. 10451–10453.

[11] Kin Fai Mak and Jie Shan. "Photonics and Optoelectronics of 2D Semiconductor Transition Metal Dichalcogenides". In: *Nature Photonics* 10 (Mar. 2016), pp. 216–226. DOI: DOI:10.1038/NPHOTON.2015.282.

[12] A. Kuc, N. Zibouche, and T. Heine. "Influence of Quantum Confinement on the Electronic Structure of the Transition Metal Sulfide TS_2". In: *Phys. Rev. B* 83.24 (June 2011), p. 245213. DOI: 10.1103/PhysRevB.83.245213. URL: https://link.aps.org/doi/10.1103/PhysRevB.83.245213.

[13] Kin Fai Mak et al. "Atomically Thin MoS $_2$: A New Direct-Gap Semiconductor". In: *Physical Review Letters* 105.13 (2010), p. 136805.

[14] Andrea Splendiani et al. "Emerging Photoluminescence in Monolayer MoS2". In: *Nano letters* 10.4 (2010), pp. 1271–75.

[15] E. Benavente et al. "Intercalation Chemistry of Molybdenum Disulfide". In: *Coordination Chemistry Reviews* 224.1 (2002), pp. 87–109. ISSN: 0010-8545. DOI: https://doi.org/10.1016/S0010-8545(01)00392-7. URL: http://www.sciencedirect.com/science/article/pii/S0010854501003927.

[16] Tawinan Cheiwchanchamnangij and W Lambrecht. "Quasiparticle Band Structure Calculation of Monolayer, Bilayer, and Bulk MoS2". In: *Physical Review B* 85 (May 2, 2012), p. 205302. DOI: 10.1103/PhysRevB.85.205302.

[17] Kin Fai Mak et al. "Tightly Bound Trions in Monolayer MoS2". In: *Nature Materials* 12.3 (Mar. 2013), pp. 207–211. ISSN: 1476-1122. DOI: 10.1038/nmat3505. URL: http://www.nature.com/nmat/journal/v12/n3/full/nmat3505.html?foxtrotcallback=true (visited on 09/29/2017).

[18] Yumeng You et al. "Observation of Biexcitons in Monolayer WSe2". In: *Nat Phys* 11.6 (June 2015). Letter, pp. 477–481. ISSN: 1745-2473. URL: http://dx.doi.org/10.1038/nphys3324.

[19] Jingzhi Shang et al. "Observation of Excitonic Fine Structure in a 2D Transition-Metal Dichalcogenide Semiconductor". In: *ACS Nano* 9.1 (2015), pp. 647–655. DOI: 10.1021/nn5059908. pmid: 25560634. URL: http://dx.doi.org/10.1021/nn5059908.

[20] A. Thilagam. "Exciton Complexes in Low Dimensional Transition Metal Dichalcogenides". In: *Journal of Applied Physics* 116.5 (Aug. 7, 2014), p. 053523. ISSN: 0021-8979, 1089-7550. DOI: 10.1063/1.4892488. URL: http://aip.scitation.org/doi/10.1063/1.4892488 (visited on 11/02/2017).

[21] Freddy T. Rabouw and Celso de Mello Donega. "Excited-State Dynamics in Colloidal Semiconductor Nanocrystals". In: *Topics in Current Chemistry* 374.5 (Aug. 2016), p. 58. ISSN: 2364-8961. DOI: 10.1007/s41061-016-0060-0. URL: https://doi.org/10.1007/s41061-016-0060-0.

[22] *Center for Integrated Nanostruture Physics (CINAP)*. URL: http://cinap.ibs.re.kr/html/cinap_en/ (visited on 10/31/2017).

[23] Claudia Ruppert, Ozgur Burak Aslan, and Tony F. Heinz. "Optical Properties and Band Gap of Single- and Few-Layer MoTe2 Crystals". In: *Nano Letters* 14.11 (Nov. 12, 2014), pp. 6231–6236. ISSN: 1530-6992. DOI: 10.1021/nl502557g. pmid: 25302768.

[24] J.A. Wilson and A.D. Yoffe. "The Transition Metal Dichalcogenides Discussion and Interpretation of the Observed Optical, Electrical and Structural Properties". In: *Advances in Physics* 18.73 (May 1969), pp. 193–335. ISSN: 0001-8732, 1460-6976. DOI: 10.1080/00018736900101307. URL: http://www.tandfonline.com/doi/abs/10.1080/00018736900101307 (visited on 11/01/2017).

[25] T. Korn et al. "Low-Temperature Photocarrier Dynamics in Monolayer MoS_2". In: *Applied Physics Letters* 99.10, 102109 (Sept. 2011), p. 102109. DOI: 10.1063/1.3636402.

[26] Maurizia Palummo, Marco Bernardi, and Jeffrey C. Grossman. "Exciton Radiative Lifetimes in Two-Dimensional Transition Metal Dichalcogenides". In: *Nano Letters* 15.5 (2015), pp. 2794–2800. DOI: 10.1021/nl503799t. pmid: 25798735. URL: http://dx.doi.org/10.1021/nl503799t.

[27] Duy Le et al. "Spin–orbit Coupling in the Band Structure of Monolayer WSe 2". In: *Journal of Physics: Condensed Matter* 27.18 (2015), p. 182201. ISSN: 0953-8984. DOI: 10.1088/0953-8984/27/18/182201. URL: http://stacks.iop.org/0953-8984/27/i=18/a=182201 (visited on 10/11/2017).

[28] Chendong Zhang et al. "Probing Critical Point Energies of Transition Metal Dichalcogenides: Surprising Indirect Gap of Single Layer WSe_2". In: *Nano Letters* 15.10 (Oct. 14, 2015), pp. 6494–6500. ISSN: 1530-6984, 1530-6992. DOI: 10.1021/acs.nanolett.5b01968. URL: http://pubs.acs.org/doi/10.1021/acs.nanolett.5b01968 (visited on 11/02/2017).

[29] B. Amin, T. P. Kaloni, and U. Schwingenschlögl. "Strain Engineering of WS_2, WSe_2, and WTe_2". In: *RSC Advances* 4.65 (Aug. 12, 2014), p. 34561. ISSN: 2046-2069. DOI: 10.1039/C4RA06378C. URL: http://xlink.rsc.org/?DOI=C4RA06378C (visited on 11/02/2017).

[30] Ajit Srivastava et al. "Valley Zeeman Effect in Elementary Optical Excitations of a Monolayer WSe2". In: *Nature Physics* 11.2 (Jan. 26, 2015), pp. 141–147. ISSN: 1745-2473, 1745-2481. DOI: 10.1038/nphys3203. arXiv: 1407.2624. URL: http://arxiv.org/abs/1407.2624 (visited on 10/10/2017).

[31] Jing-Kai Huang et al. "Large-Area Synthesis of Highly Crystalline WSe_2 Monolayers and Device Applications." In: *ACS nano* 8.1 (Jan. 2014), pp. 923–30. DOI: 10.1021/nn405719x. pmid: 24328329.

[32] J. Ribeiro-Soares et al. “Group Theory Analysis of Phonons in Two-Dimensional Transition Metal Dichalcogenides”. In: *Physical Review B* 90.11 (Sept. 29, 2014). ISSN: 1098-0121, 1550-235X. DOI: 10.1103/PhysRevB.90.115438. arXiv: 1407.1226. URL: http://arxiv.org/abs/1407.1226 (visited on 11/07/2017).

[33] H. Katzke, P. Tolédano, and W. Depmeier. “Phase Transitions between Polytypes and Intralayer Superstructures in Transition Metal Dichalcogenides”. In: *Physical Review B* 69.13 (Apr. 22, 2004), p. 134111. DOI: 10.1103/PhysRevB.69.134111. URL: https://link.aps.org/doi/10.1103/PhysRevB.69.134111 (visited on 11/07/2017).

[34] A. Schenk. “A Model for the Field and Temperature Dependence of Shockley-Read-Hall Lifetimes in Silicon”. In: *Solid-State Electronics* 35.11 (Nov. 1992), pp. 1585–1596. ISSN: 00381101. DOI: 10.1016/0038-1101(92)90184-E. URL: http://linkinghub.elsevier.com/retrieve/pii/003811019290184E (visited on 11/02/2017).

Acknowledgement

I would like to express my gratitude towards some of the many people who provided me with support in the work on this thesis. Firstly, I would like to thank Professor Schilling for his help in coordinating this master thesis abroad. Secondly, the whole group of Professor Gregorkiewicz at the UvA deserves many thanks for providing the opportunity to carry out this work and all the fruitful discussions and tips, be it related to work or not. I want to specifically mention Dr. Capretti, who has supervised me and soon-to-be-Dr. Lesage for all the time he has spent with me explaining and debugging the experiments. A further thanks goes out to my parents for their loving belief in me and material support.

The greatest thanks of all goes out to Hanin, who has filled the often gray days in Amsterdam with colour.